


# Surface Waveguide and Y Splitter Enabled by Complementary Impedance Surfaces

Kazem Zafari<sup>✉\*</sup> and Homayoon Oraizi<sup>✉†</sup>

*Department of Electrical Engineering, Iran University of Science and Technology, 1684613114 Tehran, Iran*

 (Received 14 October 2019; revised manuscript received 10 March 2020; accepted 28 April 2020; published 11 June 2020)

This paper presents a low-loss and broadband impedance-interface waveguide and a broadband mode-matching technique to convert transverse electromagnetic (TEM) mode into line-wave (LW) mode, which is formed at the interface between two complementary impedance surfaces. Furthermore, an ultra-wideband Y splitter is designed based on the one-dimensional (1D) impedance-interface waveguides. Broad bandwidth, low loss, tunable mode confinement, and ability for integration are the benefits of 1D impedance-interface waveguides. However, their drawbacks may stem from the lack of and problematic excitation of a pure LW mode at the interface between two planes. Another limitation is the coupling efficiency between 1D impedance-interface waveguides and conventional microwave waveguides. To ratify such limitations, a broadband tapered-slot Vivaldi transition is designed to excite the proposed 1D impedance-interface waveguide. Subsequently, a Y splitter consisting of complementary impedance surfaces is designed, fabricated, and measured. The Y splitter is implemented in the frequency band of 4–16 GHz, having a bandwidth of 120% and an insertion loss of approximately 1 dB. The aforementioned characteristics of 1D impedance-interface waveguides are fully verified. Consequently, the proposed waveguide, mode-matching technique, and Y splitter could be used for the design of other microwave devices.

DOI: [10.1103/PhysRevApplied.13.064025](https://doi.org/10.1103/PhysRevApplied.13.064025)

## I. INTRODUCTION

Surface waves (SWs) possessing interesting features have received significant attention over the last two decades. Surface waves can be excited at the interface between two materials having different permittivities and may propagate along the interface while decaying exponentially in the direction perpendicular to the interface [1]. At optical frequencies these waves are known as surface plasmons. Many waveguides have been designed by applying SWs at the interfaces of different media. Goubau lines [2] support SWs at the interface of metals and dielectrics, the same as spoof surface plasmons [3]. In addition, SWs can propagate at the interface of dielectrics with different permittivities [4]. Applying the idea that the wavevector can be manipulated by the local intensity of guided waves, nonlinear waveguides have been designed for optical signal processing systems [5].

It has been reported that by placing two different media adjacent to each other or through changing the structure of the interface surface, the properties of surface waves can be controlled [6,7]. Several studies, for instance, Refs. [8–10],

have shown the possibility of manipulating the phase and group velocity of SWs by developing metasurface unit cells with the desired surface impedance. In other words, the metasurface unit cells should be patterned in some required manners for guiding or splitting SWs in certain directions. By changing the sizes and shapes of the metasurface unit cells, different surface impedances can be realized. Consequently, the surface can be patterned to realize many functions. Surface waves have been broadly used in order to design microwave components and antennas including waveguides, splitters, sensors, power dividers, antenna feed, and leaky-wave antennas [11,12]. Furthermore, they are valuable to realize subwavelength guiding structures, sensing applications, and high-density integration of optical circuits [13,14].

Recently, several studies have concentrated on the structures with interface modes presenting robustness with wave-vector-locked states and field confinement [15]. For instance, a waveguide has been developed in which the electromagnetic wave propagates along an arbitrary one-dimensional (1D) line at the interface between two impedance surfaces [16]. As the wave is confined at an arbitrary 1D line, the term “line wave” (LW) has been appropriately used by Bisharat *et al.* [16]. The fundamental features of LWs can be listed as follows: field singularity at the line, unidirectional propagation behavior, robust

\*zafarikazem@yahoo.com

†h\_oraizi@iust.ac.ir

wave-vector-locked states, broad bandwidth, and tunable mode confinement.

In another study, Xu *et al.* [17] reported a broadband adiabatic transition between conventional microwave transmission lines and 1D impedance-interface waveguides. Although these studies [16,17] have many advantages, it seems that they suffer from several limitations. In Ref. [16], the LW mode is excited by a probe antenna oriented along the interface. A weakness of this method is the low-level coupling efficiency between the probe antenna and the 1D impedance-interface waveguide. A drawback associated with the proposed waveguide by Xu *et al.* [17] is the propagation of surface waves in any direction on the two surrounding adjacent impedance surfaces. As a result, the insertion loss of this waveguide is high. Due to the unique characteristics and properties of impedance-interface waveguides and their aforementioned limitations, it is required to devise alternative structures and mode-matching techniques for the improvement of their performance.

In this paper, a surface-wave Y splitter composed of complementary impedance surfaces is proposed. In order to realize the Y splitter, a low-loss and broadband 1D impedance-interface waveguide is first presented. Next, a broadband tapered-slot Vivaldi transition is developed between the conventional microwave waveguide and the proposed 1D impedance-interface waveguide. The proposed Y splitter consists of three sections, each section composed of a transverse-electric (TE) surface surrounded by two transverse-magnetic (TM) surfaces. The transmission-line model is used to design the proposed Y splitter. An example of the Y splitter is designed, fabricated, and measured. A satisfactory agreement between the simulation and measurement results confirms the practicality of the proposed solution. The ultra wideband, low loss, stable performance, and its integration ability are the key benefits of the proposed Y splitter. The implementation of the proposed Y splitter shows that complementary impedance surfaces can be employed to design other devices in other regimes, such as integrated photonics, sensing, switching, reconfigurable waveguides, and phase shifters. This paper is organized as follows: Sec. II reviews impedance-interface waveguides and their properties. In Sec. III, the proposed Y splitter is developed. Section IV highlights the fabrication results of the proposed Y splitter. Finally, a brief conclusion is made in Sec. V.

## II. TM-TE IMPEDANCE-INTERFACE WAVEGUIDES

An inexpensive method to realize impedance surfaces is the use of printed periodic patches and grids on a dielectric substrate, which may be grounded or ungrounded. These surfaces behave inductively or capacitively depending on

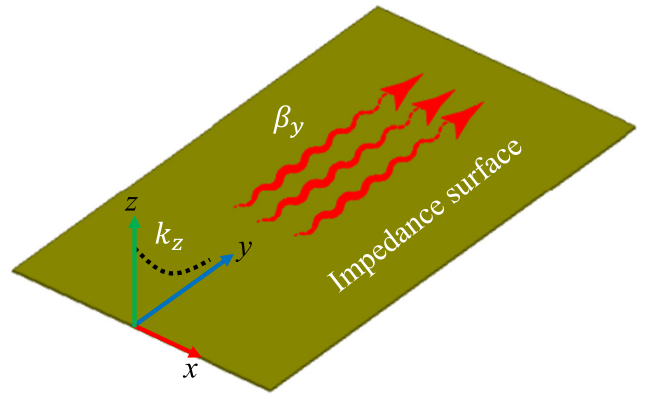


FIG. 1. Surface wave propagating along the  $+y$  direction on a plane impedance surface.

the shape of unit cells. As shown in Fig. 1, consider a lossless and homogeneous impedance surface on which a surface wave propagates in the  $y$  direction. The  $z$  components of the electromagnetic field can be represented as

$$E_z = E_0 e^{-j\beta_y y - k_z z}, \quad (1)$$

$$H_z = H_0 e^{-j\beta_y y - k_z z}, \quad (2)$$

where  $\beta_y$  and  $k_z$  are the phase and decay constants of the surface wave, respectively. For impedance surfaces, parameters such as surface impedance and propagation impedance are defined. The propagation impedance is the ratio of the field components, whose Poynting vector is towards the propagation direction, and the surface impedance is defined as the ratio of the tangential field components on the surface. For the TM mode, the surface and propagation impedances are defined as [18,19]

$$Z_{\text{prop}}^{\text{TM}} = \frac{E_z}{H_x} = \frac{\beta_y Z_0}{k_0} = n Z_0, \quad (3)$$

$$Z_{\text{surf}}^{\text{TM}} = \frac{-E_y}{H_x} = \frac{j k_z Z_0}{k_0} = \frac{j Z_0}{\zeta}. \quad (4)$$

Similarly for the TE mode, the surface and propagation impedances can be expressed as

$$Z_{\text{prop}}^{\text{TE}} = \frac{-E_x}{H_z} = \frac{k_0 Z_0}{\beta_y} = \frac{Z_0}{n}, \quad (5)$$

$$Z_{\text{surf}}^{\text{TE}} = \frac{E_x}{H_y} = \frac{-j k_0 Z_0}{k_z} = -j Z_0 \zeta, \quad (6)$$

where  $k_0$  and  $Z_0$  are the wave number and the intrinsic impedance in the free space above the surface,  $n = \beta_y/k_0$

is the refraction index, and  $\zeta = k_0/k_z = 1/\sqrt{n^2 - 1}$  is a real positive number. Based on Eqs. (4) and (6), the surface impedances should be inductive and capacitive to support TM and TE modes, respectively [20,21].

The 1D impedance-interface waveguide was proposed by Bisharat *et al.* [16]. In this case, the impedance surfaces confining the electromagnetic wave should have complementary impedance surfaces. Due to the complementary boundary conditions in such surfaces, one of the surfaces should support a TM mode while the other should support a TE mode. The dual wave behavior in such inductive and capacitive surfaces leads to a new mode, which is a result of the interference between the TM and TE modes at the interface. The condition of the propagation of such a mode is the equality of the phase velocities of TM-polarized and TE-polarized surface waves. If the phase velocities in both TM and TE surfaces are equal, the product of the TM and TE surface impedances in Eqs. (4) and (6) is [14,16]

$$Z_{\text{surf}}^{\text{TM}} Z_{\text{surf}}^{\text{TE}} = \eta_0^2. \quad (7)$$

According to Eqs. (4) and (6), the choice  $\zeta$  equal to infinity renders the TM and TE surfaces to the perfect electric conductor (PEC) and perfect magnetic conductor (PMC) surfaces. The tangential electric (magnetic) field is zero in the PEC (PMC) surface, thus allowing only the TM (TE) mode to propagate. When interfacing these surfaces, the LW mode is formed at the interface due to the dual behavior of wave in such surfaces. The LW formation between the adjacent PEC and PMC surfaces is evident in Fig. 2(a). The magnitude and vector distributions of the electric field, which are obtained by the eigenmode solver of ANSYS HFSS software on the  $z$ - $o$ - $x$  plane perpendicular to the direction of propagation are shown in Fig. 2(b). As illustrated in Fig. 2(b), the  $E$  field has a component toward the normal direction on the PEC surface and varies gradually toward the transverse direction on the PMC surface.

The decay constants,  $k_z$ , of TE and TM modes are inversely proportional to  $\zeta$ . Consequently, the LW mode

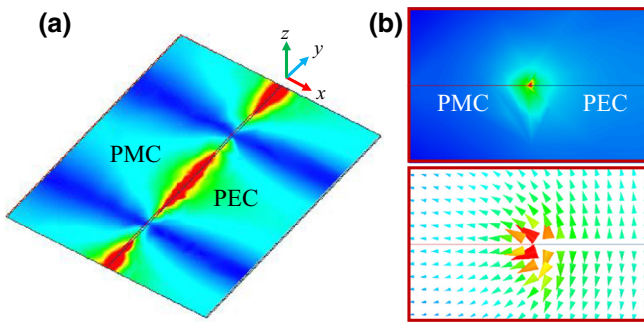


FIG. 2. (a) Line-wave mode formation between the PEC and PMC surfaces. (b) Magnitude and vector distributions of the electric field on the  $z$ - $o$ - $x$  plane.

generated at the interface between the PEC-PMC surfaces supports the surface wave, which has weak confinement and is loosely bound to the surface. However, a more tightly bound mode can be attainable by using a finite value for  $\zeta$  and hence  $\beta > k_0$ . Consequently, the tunable mode confinement by the value of  $\zeta$  is one of the properties of LW modes [16].

In order to realize the LW mode, two surface impedances are required, namely an inductive (capacitive) surface to support a TM (TE) mode. The metasurfaces can support TE and TM modes or combinations of them according to their geometrical structures. In general, the dominant TM mode may be generated by metasurfaces composed of subwavelength cells printed on grounded substrates, irrespective of being of patch or aperture type [14,22]. However, for the ungrounded substrates, the electromagnetic behavior of the metasurface depends on the geometry of unit cells. At low frequencies (small dimensions of unit cells relative to the wavelength), the connection of adjacent cells by metallic lines converts the dominant mode from TE to TM [23]. The gaps between the adjacent conducting patches of ungrounded patch-type metasurfaces create a dominant capacitive response at low frequencies.

As analyzed in Eqs. (4) and (6), a capacitive response is needed to support the dominant TE mode. The ungrounded aperture-type metasurfaces are the complementary geometries of the ungrounded patch-type metasurfaces (whose surface impedances are capacitive). Consequently, according to the Babinet principle, their surface impedances are inductive. In fact, the inductance mainly comes from the continuous conducting strips [14,22].

The patch-type and aperture-type metasurfaces are shown in Figs. 3(a) and 3(b). The periodic constants in the directions of  $x$  and  $y$  are  $P_x = 1$  mm and  $P_y = 2$  mm. The geometric parameters of the unit cells  $a$  and  $b$  are 0.6 mm and 1.7 mm, respectively. The substrate Rogers RT \duriod 6010 (with dielectric constant 10.5 and thickness 20 mil) is used for the ungrounded unit cells.

The eigenmode solver of CST Microwave Studio can be used to obtain the vector distributions of the electric and magnetic fields on arbitrarily shaped unit cells. For the patch-type unit cell, the vector distribution of the electric and magnetic fields in the  $z$ - $o$ - $x$  plane perpendicular to the direction of propagation and the magnetic field in the  $z$ - $o$ - $y$  plane for the phases  $\phi_x = 0$  and  $\phi_y = 45$  in the  $x$  and  $y$  directions are presented in Fig. 4(a). This mode has transverse components of electric and magnetic fields, ( $E_x \neq 0, H_z \neq 0$ ), and longitudinal component of magnetic field, ( $H_y \neq 0$ ). Therefore, the propagated wave for the patch-type unit cell is TE mode. Likewise, for the aperture-type unit cell the vector distributions of the magnetic and electric fields in the  $z$ - $o$ - $x$  and  $z$ - $o$ - $y$  planes are presented in Fig. 4(b). This mode has the transverse components of electric and magnetic fields, ( $E_z \neq 0, H_x \neq 0$ ),

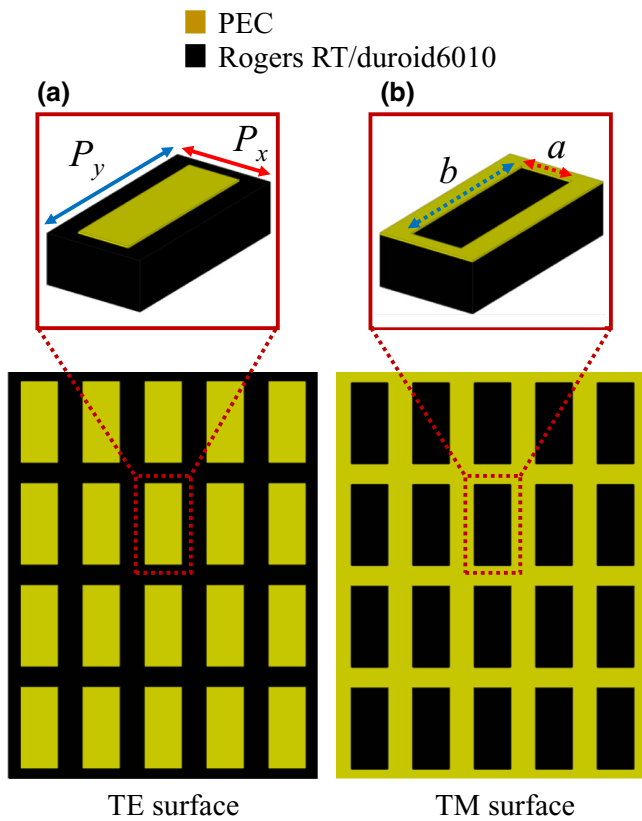


FIG. 3. Complementary impedance surfaces. (a) Patch-type impedance surface that supports the TE mode. (b) Aperture-type impedance surface that supports the TM mode. Inserts show the unit cells of TE and TM surfaces with the geometrical parameters of  $P_x = 1$  mm,  $P_y = 2$  mm,  $a = 0.5$  mm, and  $b = 1.6$  mm.

and longitudinal component of electric field, ( $E_y \neq 0$ ). As a result, the TM mode propagates in the aperture-type unit cell [24].

The dispersion curves of the proposed unit cells of TE and TM surfaces, which are obtained by the eigenmode solver of CST Microwave Studio are shown in Fig. 5. As illustrated, the TM and TE modes have the dispersion curves that overlap over a wide frequency range as desired. To better understand the mechanisms of 1D impedance-interface waveguides, based on how TE and TM impedance surfaces are located, three structures can be assumed for these waveguides: waveguide I, waveguide II, and waveguide III. Waveguide I comprises two side-by-side complementary TE and TM surface impedances. Waveguide II comprises a TM impedance surface surrounded by two TE impedance surfaces. Waveguide III comprises a TE impedance surface surrounded by two TM impedance surfaces.

Waveguide I having widths  $W_{TM,I} = 16$  mm and  $W_{TE,I} = 16$  mm for TM and TE surfaces is shown in Fig. 6(a). Its electric field vector distribution is presented in Fig. 6(a). The electric field vector is perpendicular and

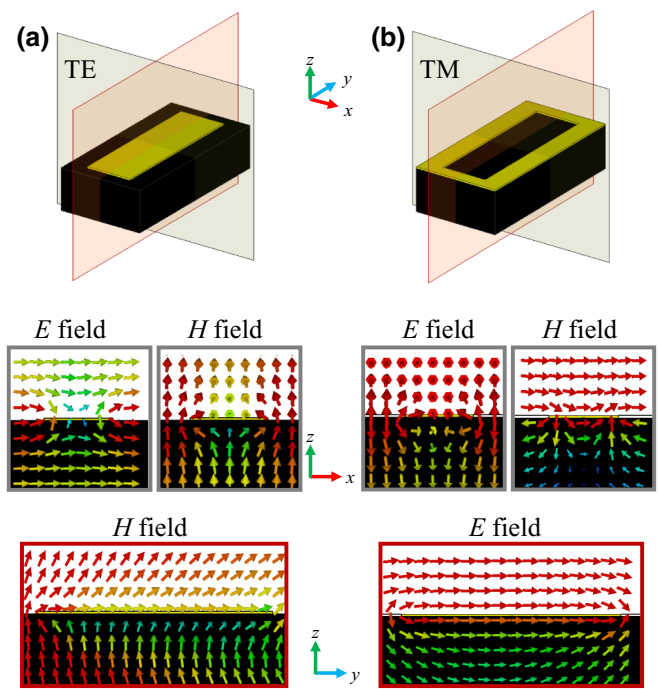


FIG. 4. (a) Vector distributions of the electric and magnetic fields in the  $z$ - $o$ - $x$  plane and the vector distribution of the magnetic field in the  $z$ - $o$ - $y$  plane for the patch-type impedance surface. (b) Vector distributions of the electric and magnetic fields in the  $z$ - $o$ - $x$  plane and the vector distribution of the electric field in the  $z$ - $o$ - $y$  plane for the aperture-type impedance surface.

tangential to the TM and TE impedance surfaces, respectively. Such orientations of the electric field vectors at the TM and TE impedance surfaces verify the existence of the LW mode at the interface. Waveguides II and III with surface widths  $W_{TE,II} = 14$  mm,  $W_{TM,II} = 5$  mm, and  $W_{TM,III} = 14$  mm,  $W_{TE,III} = 5$  mm can be seen in Figs. 6(b)

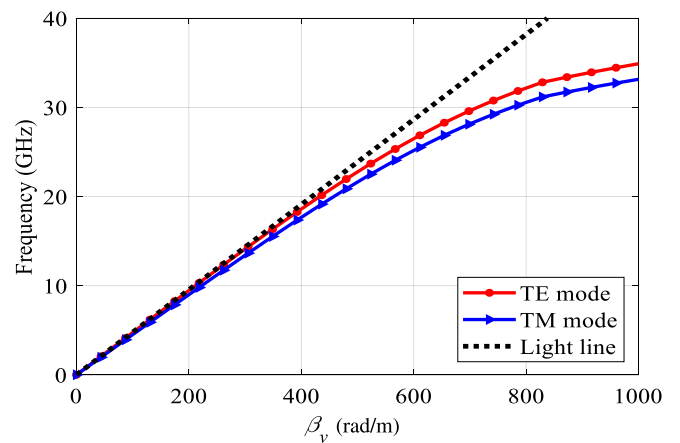


FIG. 5. Dispersion curves of the proposed unit cells of TE and TM surfaces with the geometrical parameters of  $P_x = 1$  mm,  $P_y = 2$  mm,  $a = 0.5$  mm, and  $b = 1.6$  mm.



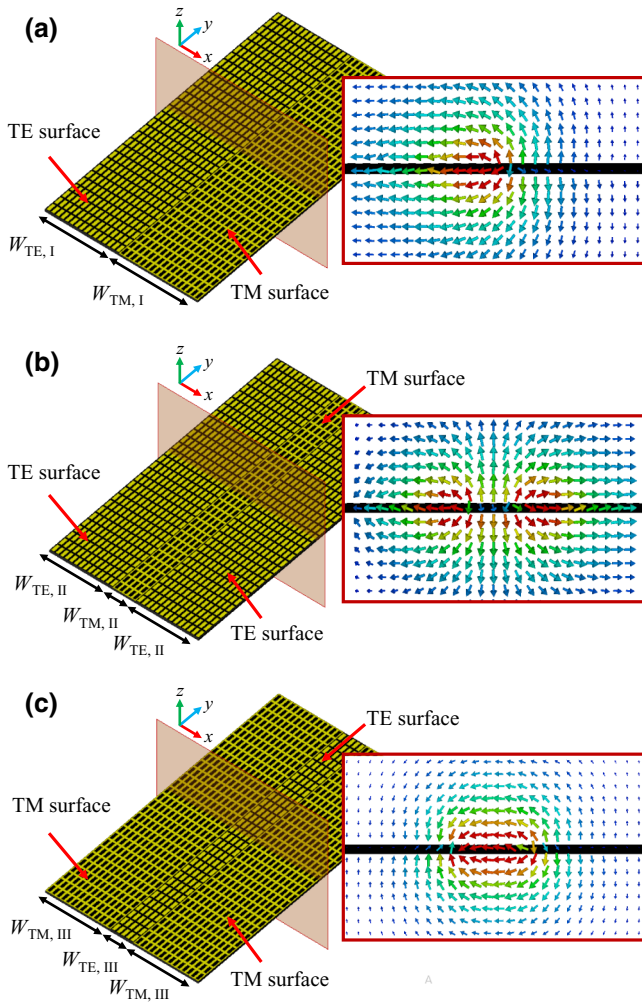


FIG. 6. Schematic configurations of impedance-interface waveguides. (a) Waveguide I, which consists of two side-by-side complementary surface impedances. (b) Waveguide II, which consists of a TM impedance surface surrounded by two TE impedance surfaces. (c) Waveguide III, which is composed of a TE impedance surface surrounded by two TM impedance surfaces, where the inserts show the electric field vector distributions in the  $z$ - $o$ - $x$  plane.

and 6(c), respectively. The electric field vector distributions of these waveguides are displayed in Figs. 6(b) and 6(c).

For a two-port network, the scattering parameter  $S_{11}$  is defined as the reflection coefficient at the input port (port 1) when the output port (port 2) is matched (terminated by the matched load) and the scattering parameter  $S_{21}$  is defined as the forward transmission (from port 1 to port 2) when the output port is matched [24]. The diagrams of scattering parameters  $S_{11}$  and  $S_{21}$  simulated in CST Microwave Studio for three waveguides are shown in Figs. 7(a) and 7(b), respectively. In the simulations, the waveguide ports are utilized for the excitation of 1D impedance-interface waveguides. Observe that waveguide

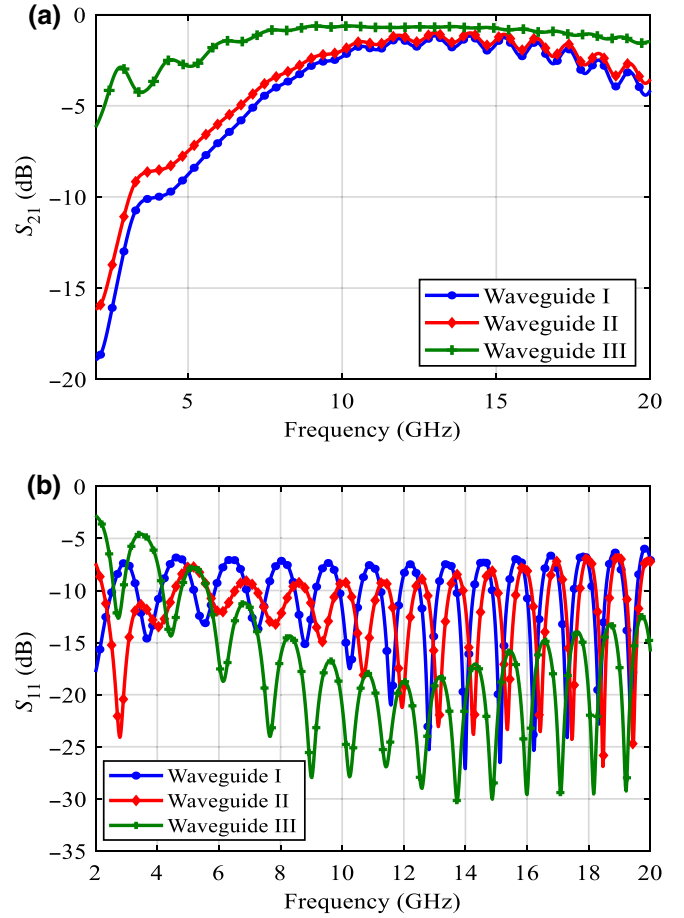


FIG. 7. Scattering parameters of 1D impedance-interface waveguides. (a) Simulated  $S_{21}$  and (b)  $S_{11}$  of waveguide I, waveguide II, and waveguide III.

III has lower insertion loss and wider bandwidth than waveguides I and II.

For a better understanding of the difference among the insertion losses of three waveguides, their electric field distributions at 10 and 18 GHz are presented in Figs. 8(a)–8(f). It is observed from Fig. 4 that in the cases of waveguides I and II, the wave is not totally confined at the interface and propagates in different directions on the TE surfaces, while in waveguide III the wave is confined between the TM surfaces. Therefore, the insertion losses of waveguides I and II have been increased under the effect of the wave propagation in undesired directions.

The TE and TM surface impedances ( $Z_{\text{surf}}$ ) used to generate the LW mode are complex (with wave vector  $k = \beta - j\alpha$ ) due to the losses. The attenuation constant,  $\alpha$ , on the surface can be calculated by the surface impedance and method in Ref. [25]. The surface impedance can be analytically determined by the transverse resonance equation on the basis of equivalent circuit model [11]. In fact, the surface-wave mode is characterized by simulations of space-wave mode. Details of finding the attenuation constants of the TE and TM surfaces are described here.

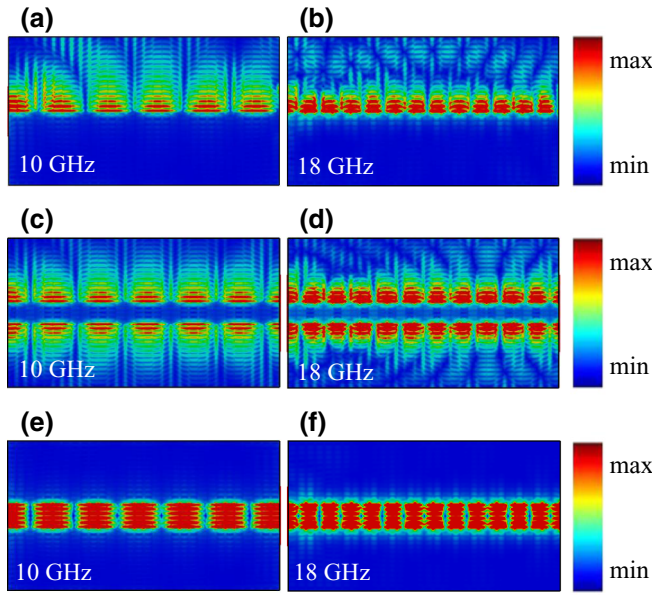


FIG. 8. (a),(b) Electric field distributions of waveguide I at 10 and 18 GHz. (c),(d) Electric field distributions of waveguide II at 10 and 18 GHz. (e),(f) Electric field distributions of waveguide III at 10 and 18 GHz.

(1) The first step is to obtain the sheet impedance,  $Z_{\text{sheet}}$ , of each unit cell from a normal-incidence scattering simulation, such as a Floquet simulation in CST Microwave Studio. As shown in Fig. 9(a), proper boundary conditions

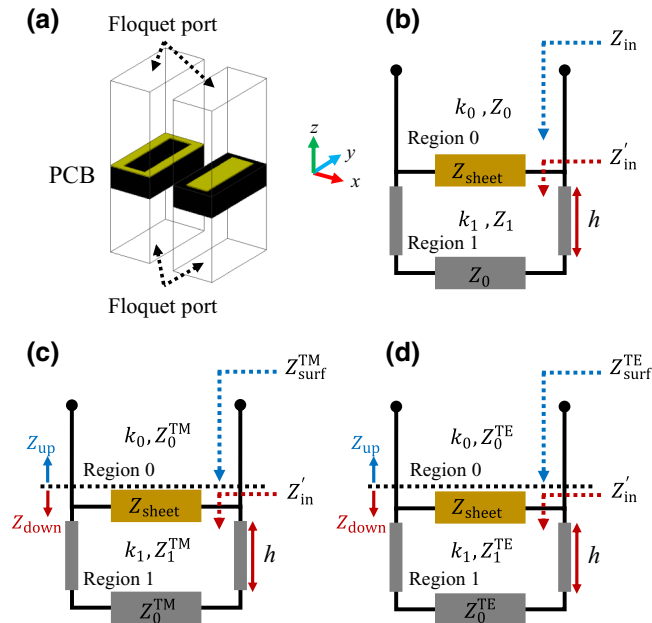


FIG. 9. (a) Floquet simulation performed on the TM and TE unit cells to find the sheet impedance. (b) Transmission-line model of the TM and TE unit cells. (c) Modified transmission-line model of the TM modal impedance. (d) Modified transmission-line model of the TE modal impedance.

are applied in the simulation. Periodic boundary conditions in the  $x$  and  $y$  directions are assumed. The Floquet ports are located at  $z = \pm\lambda$  as the incident waves. The transmission-line model of these unit cells is illustrated in Fig. 9(b), where the PEC top layer is represented as the sheet impedance,  $Z_{\text{sheet}}$ , and the substrate is modeled as a transmission line with the characteristic impedance  $Z_1$  and load  $Z_0$ . Based on the knowledge of microwave engineering [24], the input impedance,  $Z_{\text{in}}$ , can be determined by the simulated reflection coefficient  $S_{11}$  of space-wave mode as

$$Z_{\text{in}} = Z_0 \frac{1 + S_{11}}{1 - S_{11}}. \quad (8)$$

Then the sheet impedance,  $Z_{\text{sheet}}$ , can be evaluated by

$$\frac{1}{Z_{\text{sheet}}} = \frac{1}{Z_{\text{in}}} - \frac{1}{Z_0}, \quad (9)$$

$$Z'_{\text{in}} = Z_1 \frac{Z_0 + jZ_1 \tan(k_1 h)}{Z_1 + jZ_0 \tan(k_1 h)}, \quad (10)$$

where  $k_0$  and  $Z_0$  are the characteristic wave number and impedance of free space (region 0).  $k_1 = k_0\sqrt{\epsilon_r}$  and  $Z_1 = Z_0/\sqrt{\epsilon_r}$  are the characteristic wave number and impedance of the dielectric substrate (region 1) with permittivity  $\epsilon_r$  and thickness  $h$ .

(2) Once the sheet impedances of the TE and TM unit cells have been extracted from Eq. (9), the modal surface impedances are determined by the modified transmission-line models with the wave numbers and the characteristic impedances represented by the modal wave numbers and impedances as shown in Figs. 9(c) and 9(d).

(3) According to the modified transmission-line model which is presented in Fig. 9(c), the TM surface impedance can be expressed as

$$\frac{1}{Z_{\text{surf}}^{\text{TM}}} = \frac{1}{Z_{\text{sheet}}} + \frac{1}{Z'_{\text{in}}}, \quad (11)$$

$$Z'_{\text{in}} = Z_1^{\text{TM}} \frac{Z_0^{\text{TM}} + jZ_1^{\text{TM}} \tan(k_1 h)}{Z_1^{\text{TM}} + jZ_0^{\text{TM}} \tan(k_1 h)}, \quad (12)$$

Where  $k_0$  and  $Z_0^{\text{TM}} = Z_0(k_{z0}/k_0)$  are the TM wave number and impedance of free space.  $k_1^{\text{TM}}$  and  $Z_1^{\text{TM}} = Z_1(k_{z1}^{\text{TM}}/k_1^{\text{TM}}) = Z_0 k_{z1}^{\text{TM}}/k_0 \epsilon_r$  are the TM wave number and impedance of the dielectric substrate and  $k_{z1}^{\text{TM}} = k_0 \sqrt{(\epsilon_r - 1) - (Z_{\text{surf}}^{\text{TM}}/Z_0)^2}$ . The transverse resonance technique [20] shows that, for the existence of surface-wave mode, it has to satisfy the condition  $Z_{\text{up}}(z) = -Z_{\text{down}}(z)$ .  $Z_{\text{up}}(z)$  and  $Z_{\text{down}}(z)$  constitute the impedances looking in

opposite directions from any observation plane along the transmission line. Along the reference plane (dashed line) selected in Fig. 9(c),  $Z_{\text{up}}(z) = Z_0^{\text{TM}}$  and  $Z_{\text{down}}(z) = Z_{\text{surf}}^{\text{TM}}$ . Consequently,  $Z_0^{\text{TM}} = -Z_{\text{surf}}^{\text{TM}}$ . By substituting the determined value of  $Z_{\text{sheet}}$  from Eq. (9) into Eq. (11), there is only one unknown  $Z_{\text{surf}}^{\text{TM}}$  in this equation, which can be solved by numerical tools like MATLAB. The TE surface impedance can be calculated through the same procedure as for the TM surface impedance.

$$\frac{1}{Z_{\text{surf}}^{\text{TE}}} = \frac{1}{Z_{\text{sheet}}} + \frac{1}{Z'_{\text{in}}}, \quad (13)$$

$$Z'_{\text{in}} = Z_1^{\text{TE}} \frac{Z_0^{\text{TE}} + jZ_1^{\text{TE}} \tan(k_1 h)}{Z_1^{\text{TE}} + jZ_0^{\text{TE}} \tan(k_1 h)}, \quad (14)$$

where  $k_0$  and  $Z_0^{\text{TE}} = Z_0(k_0/k_{z0})$  are the TE wave number and impedance of free space.  $k_1^{\text{TE}}$  and  $Z_1^{\text{TE}} = Z_1(k_1^{\text{TE}}/k_{z1}^{\text{TE}}) = Z_0 k_0/k_{z1}$  are the TE wave number and impedance of the dielectric substrate and  $k_{z1}^{\text{TE}} = k_0 \sqrt{(\epsilon_r - 1) - (Z_0/Z_{\text{surf}}^{\text{TE}})^2}$ ,  $Z_0^{\text{TE}} = -Z_{\text{surf}}^{\text{TE}}$ . As soon as the surface impedances are calculated, the wave numbers tangential to the surface,  $k_{\text{SW}}$ , can be determined for the TM and

TE modes through [10,16]

$$k_{\text{SW}}^{\text{TM}} = \beta_{\text{SW}}^{\text{TM}} - j\alpha_{\text{SW}}^{\text{TM}} = k_0 \sqrt{1 - \left(\frac{Z_{\text{surf}}^{\text{TM}}}{Z_0}\right)^2}, \quad (15)$$

$$k_{\text{SW}}^{\text{TE}} = \beta_{\text{SW}}^{\text{TE}} - j\alpha_{\text{SW}}^{\text{TE}} = k_0 \sqrt{1 - \left(\frac{Z_0}{Z_{\text{surf}}^{\text{TE}}}\right)^2}. \quad (16)$$

Equations (15) and (16) can be utilized to compute the attenuation constants of the TE and TM surfaces. Through the use of the  $x$ -polarized incident electric field in the Floquet simulation, the attenuation factors,  $\alpha_x/k_0$ , for the TE and TM surfaces can be calculated. The attenuation factors for the TE and TM surfaces are drawn in Fig. 10(a). Observe that the attenuation factor of the TM surface is higher than that of the TE surface. The penetration depth of the TE surface is greater than that of the TM surface, since the penetration depth for surface waves by definition is  $\delta = 1/\alpha$ , namely  $\delta_x^{\text{TE}} > \delta_x^{\text{TM}}$  [11]. Therefore, the surface wave attenuates more gradually on the TE surface than that of the TM surface.

The differences between the surface impedances and polarizations on the complementary TE and TM surfaces lead to the difference between their attenuation factors. Therefore, the performances of above waveguides I, II, and III are under the effect of the attenuation factors of thier

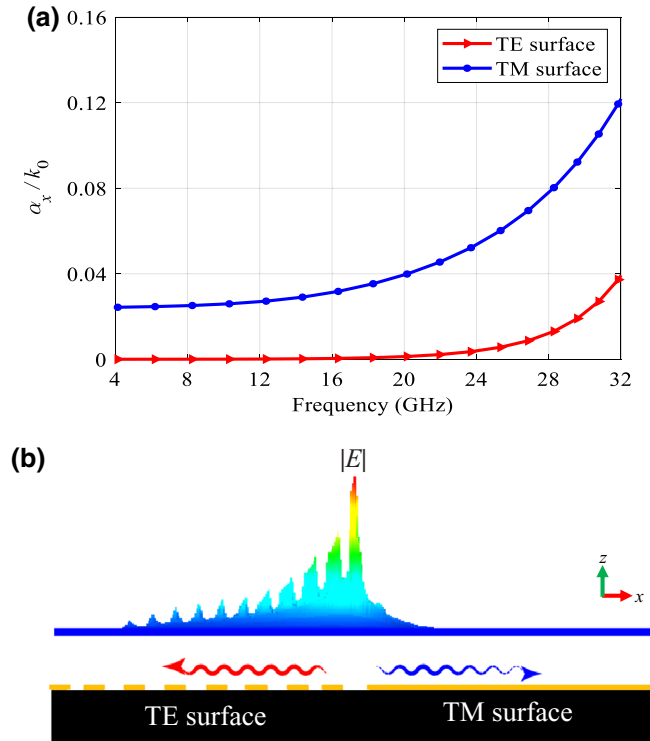


FIG. 10. (a) Attenuation factors of the TE and TM surfaces. (b) Amplitude of the electric field at frequency 10 GHz in the  $z$ - $o$ - $x$  plane for waveguide I.

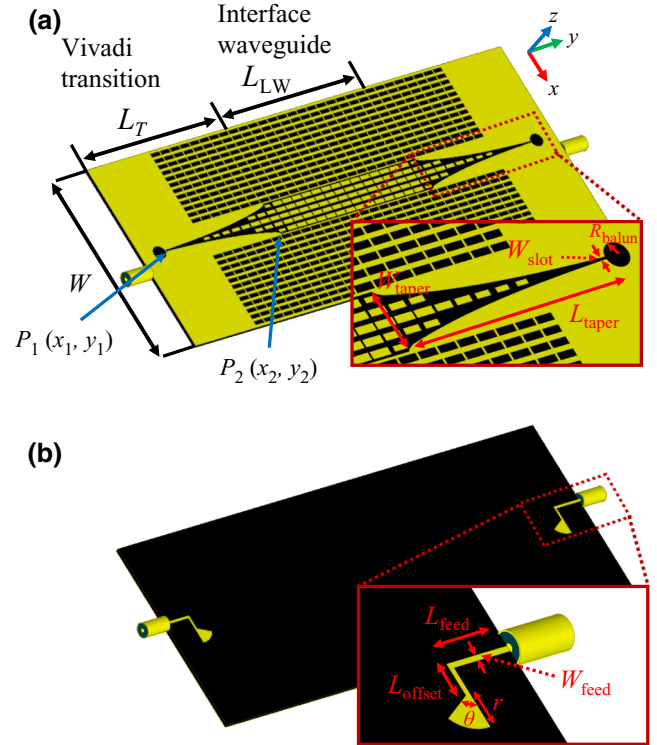


FIG. 11. Schematic configuration of the proposed TE-TM impedance-interface waveguide and Vivaldi transition. (a) Front view. (b) Back view.

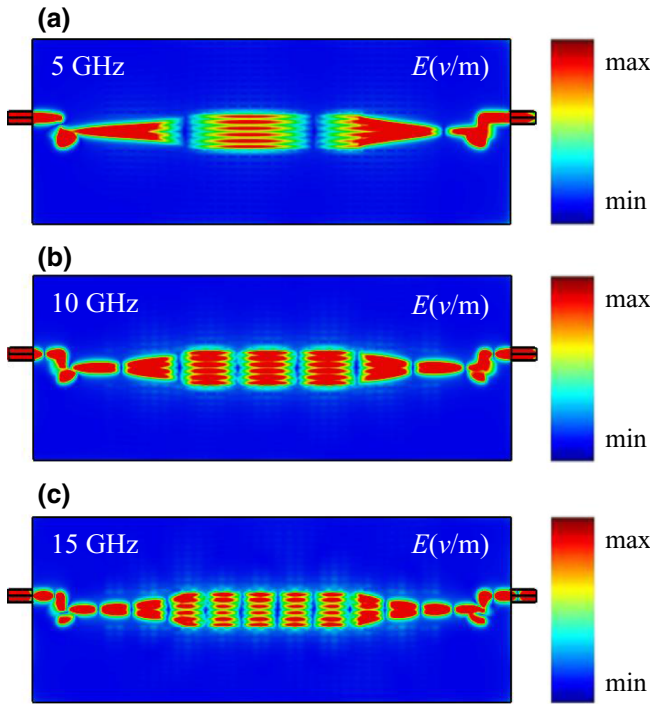


FIG. 12. (a) Simulated electric field distributions of the proposed TE-TM impedance-interface waveguide and Vivaldi transition at 5 GHz, (b) 10 GHz, and (c) 15 GHz.

impedance surfaces. For waveguide I, the amplitude of the electric field at frequency 10 GHz in the  $z$ - $o$ - $x$  plane perpendicular to the direction of wave propagation is displayed in Fig. 10(b). Observe that the amplitude of electric field for the TE surface decrease more gradually than that of the TM surface as a function of distance from the interface perpendicular to the propagation direction ( $x$  axis). As presented in Figs. 8(c) and 8(d), for waveguide II in which

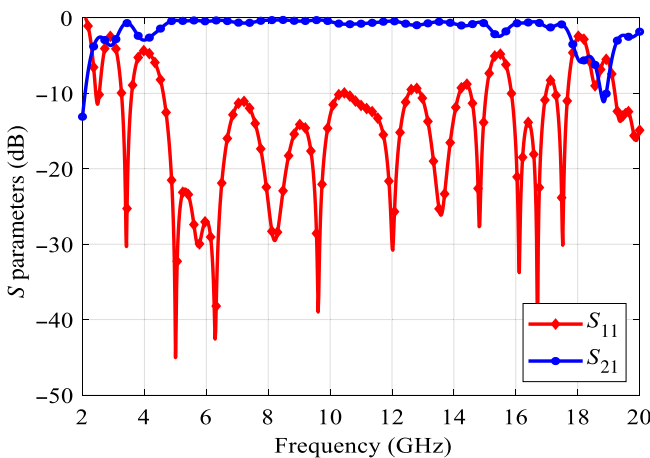


FIG. 13.  $S$  parameters of waveguide III with the Vivaldi transition.

two TE impedance surfaces surround a TM impedance surface, the surface wave gradually attenuates and spreads in any direction on the two surrounding TE surfaces. For waveguide III, since the two TM impedance surfaces with higher attenuation factors surround a TE surface, the surface wave is confined between the two TM surfaces as shown in Figs. 8(e) and 8(f).

The LW mode propagating along the 1D impedance-interface waveguides is different from the counterparts of the conventional transmission lines. Therefore, appropriate transitions are needed between these waveguides and conventional microwave transmission lines.

The design of transition for photonic and spoof surface plasmon (SSP) waveguides have been widely investigated in the literature [26,27]. The SSPs propagate with a wave number greater than  $k_0$ . Therefore, a free-space wave can hardly be converted to the SPP wave due to the momentum mismatch. Metasurfaces with specific gradient-index distributions have been designed to transform incident free-space waves to surface waves

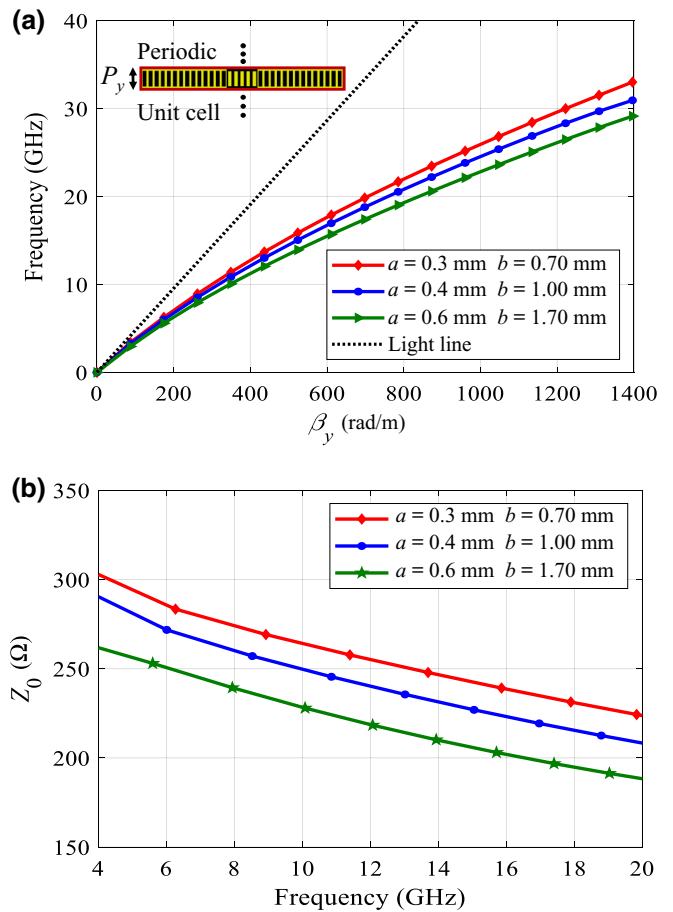


FIG. 14. (a) Dispersion diagrams of waveguide III as a function of the dimensions  $a$  and  $b$  of its unit cell. (b) Characteristic impedance of waveguide III as a function of the dimensions  $a$  and  $b$ .



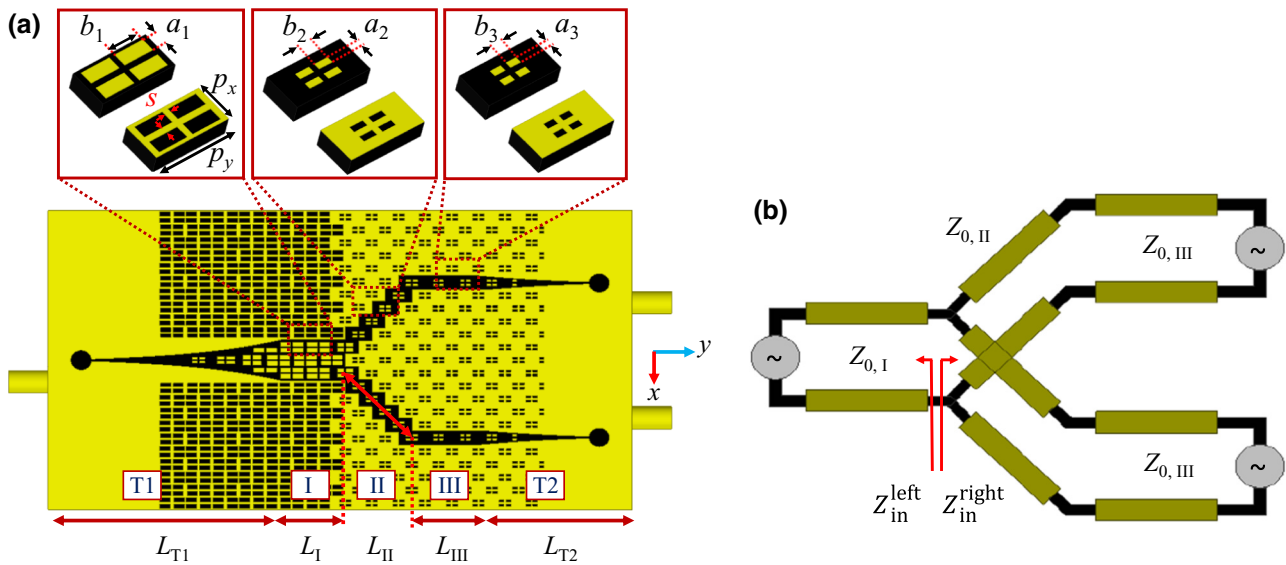


FIG. 15. (a) Schematic of the proposed Y splitter based on complementary impedance surfaces, where the insets present the detail of the TE and TM unit cells. (b) Equivalent circuit of the proposed Y splitter.

at microwave and terahertz frequencies [28,29]. Gradual changes, also known as adiabatic mode converter, were commonly used to develop the transitions from the rectangular waveguide, the coplanar waveguide, and the microstrip line to the SSPs. Passing through these structures, the primary modes smoothly transform into the target modes with low reflection within a wide frequency range [17].

Similar to the proposed method in Ref. [16] for the excitation of waveguide I, a probe antenna can be used. Its shortcomings are a low coupling efficiency and surface-wave propagation on the TE surface along undesired directions. For the excitation of waveguide II, a broadband adiabatic matching transition can be utilized, as proposed in Ref. [17]. The coupling efficiency between conventional microwave transmission lines and 1D impedance-interface waveguides has increased in this method. However, its limitation is surface-wave propagation in undesired directions on the two surrounding capacitive surfaces. As the wave is confined between the two TM surfaces in waveguide III, it is expected that utilizing an appropriate transition for this waveguide, the wave propagation in undesired directions and coupling efficiency problems can be amended.

Generally, the geometry of transition depends on the primary mode entering the transition and the target mode exiting it. For example, since the TM mode propagates in the SPP waveguides, a transition is required that transforms the TEM to the TM mode. For waveguide III, which is presented in Fig. 6(c), a transition compatible with its electric field distribution is needed to transform the TEM to the TE mode. In Ref. [30] a microstrip-to-slotline transition is introduced for transformation of TEM to TE mode to design a bandpass filter by using the SPPs. Application of

the concept of microstrip-to-slotline transition in Ref. [30] and the need for the gradual variation of transition in order to realize impedance, momentum, and mode matching, the antipodal Vivaldi transition is selected for the excitation of waveguide III. It provides the capability of transition between the TEM and TE modes.

The schematic configuration of the proposed waveguide and Vivaldi transition are presented in Fig. 11. The parameters  $W = 29$  mm,  $L_{LW} = 30$  mm, and  $L_T = 23$  mm are shown in Fig. 11. Observe that in the section above the substrate a circular cavity with radius  $R_{balun}$  is connected to the terminal flaring plane (with dimensions  $L_{taper}$ ,  $W_{taper}$ ) through a small slot with width

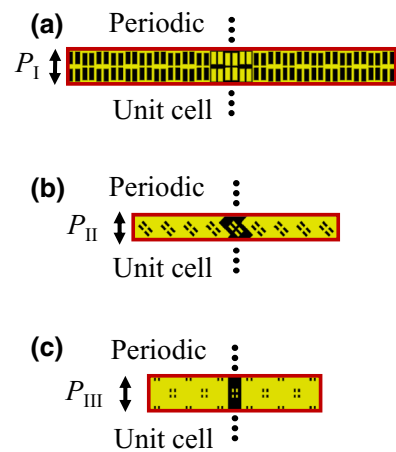


FIG. 16. (a) Schematic configuration of the unit cell of region I with the period of 2.7 mm. (b) Unit cell of region II with the period of 1.85 mm. (c) Unit cell of region III with the period of 2.7 mm.

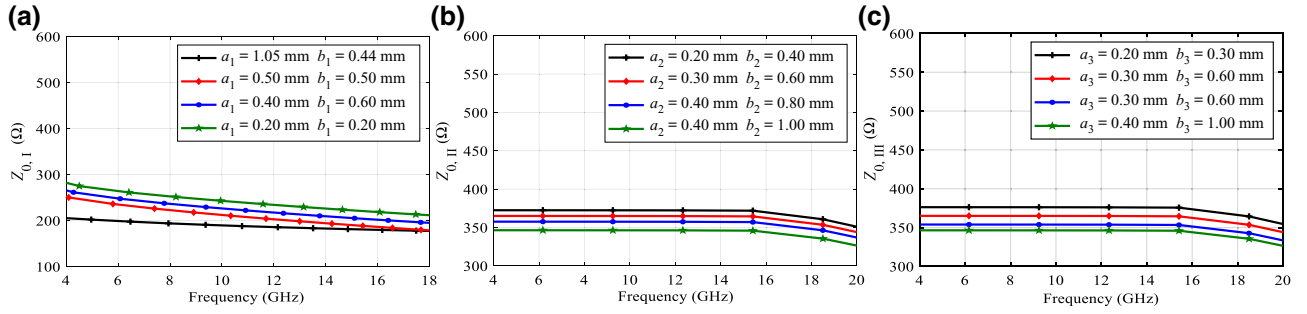


FIG. 17. (a) Characteristic impedance of region I ( $Z_{0,I}$ ) as a function of the dimensions of its patches ( $a_1, b_1$ ). (b)  $Z_{0,II}$  as a function of  $a_2$  and  $b_2$ . (c)  $Z_{0,III}$  as a function of  $a_3$  and  $b_3$ .

$W_{\text{slot}}$ . On the backside of substrate, a microstrip line exists with width  $W_{\text{feed}}$  and length  $L_{\text{feed}}$ , which is terminated by a wideband radial circular stub with radius  $r$  and angle  $\theta$ . The width of microstrip line should be  $W_{\text{feed}} = 0.35$  mm for the 50 $\Omega$  characteristic impedance. For the improvement of impedance, momentum, and mode matching, it is necessary that the dimensions of the unit cells of TE surface gradually decrease towards the narrow flaring sections. The mode converts from the TEM mode to the LW mode with a lightly altered field distribution because of the gradually changes of transition and TE unit cells along the propagation direction. The curve of flaring plane is described as  $y = C_1 e^{ax} + C_2$ , where  $C_1 = (y_2 - y_1)/(e^{ax_2} - e^{ax_1})$ ,  $C_2 = (y_1 e^{ax_1} - y_2 e^{ax_2})/(e^{ax_2} - e^{ax_1})$ , and  $a = 0.1$ .  $P_1(x_1, y_1)$  and  $P_2(x_2, y_2)$  are the starting and ending points, respectively.

After the optimization by full-wave computer simulations, the values of the aforementioned parameters are extracted as  $R_{\text{balun}} = 2$  mm,  $W_{\text{slot}} = 0.22$  mm,  $L_{\text{taper}} = 19$  mm,  $W_{\text{taper}} = 5$  mm,  $L_{\text{feed}} = 4.62$  mm,  $L_{\text{offset}} = 2.16$  mm,  $\theta = 60^\circ$ ,  $r = 2.3$  mm. The electric field distributions of waveguide III with the Vivaldi transition at 5, 10, and 15 GHz are illustrated in Fig. 12. Observe that the electric field is confined on the TE surface surrounded by two TM surfaces. The diagrams of scattering parameters  $S_{11}$  and  $S_{21}$  are shown in Fig. 13. The results of the proposed transition show that it has achieved a wideband performance with high coupling efficiency and it is quite suitable for the transformation of the TEM mode to the LW mode.

For the evaluation of the dispersion diagrams of waveguide III and the investigation of their variations as a function of the dimensions of its unit cell ( $a$  and  $b$ ), they are simulated by the eigenmode solver of CST Microwave Studio, as depicted in Fig. 14(a). In the simulation, proper boundary conditions are applied. Considering the periodicity in the  $y$  direction, periodic boundary conditions in its positive and negative directions are assumed. Perfect magnetic conductors in the  $x$ -axis directions, and also perfect electric conductors at a sufficiently far distance from the surface ( $10\lambda$ ) in the  $z$ -axis directions are assumed.

Since in waveguide III, the wave confined between two TM surfaces propagates on the TE surface, with good approximation the electric field may be considered as TE-like. Therefore, its characteristic impedance can be calculated analytically by Eq. (5). The characteristic impedance of waveguide III as a function of the dimensions  $a$  and  $b$  are shown in Fig. 14(b). The values of characteristic impedances are required for the design of the Y splitter, which is fully described in the following section.

### III. DESIGN OF Y SPLITTER

In this section, according to the results obtained in Sec. II, a Y splitter based on complementary impedance surfaces is designed and simulated. The structure of the proposed Y splitter and its equivalent circuit are shown in Figs. 15(a) and 15(b). The Y splitter is divided into five regions. Regions T1 and T2 are the input and output transitions with the lengths of  $L_{T1} = 23$  mm,  $L_{T2} = 15.5$  mm, regions I, III, and III are TM-TE impedance-interface waveguides, which have the following dimensions:  $L_I = 6.75$  mm,  $L_{II} = 7.5$  mm, and  $L_{III} = 6.75$  mm. To realize the Y splitter, complementary metasurfaces is used for the

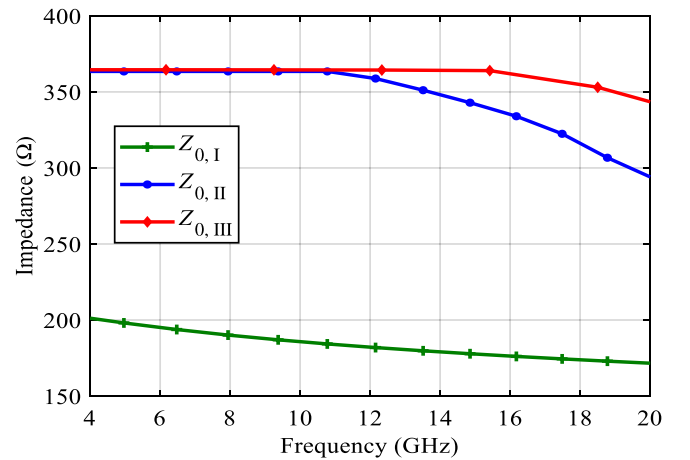


FIG. 18. Curves of the characteristic impedances of regions I, II, and III.

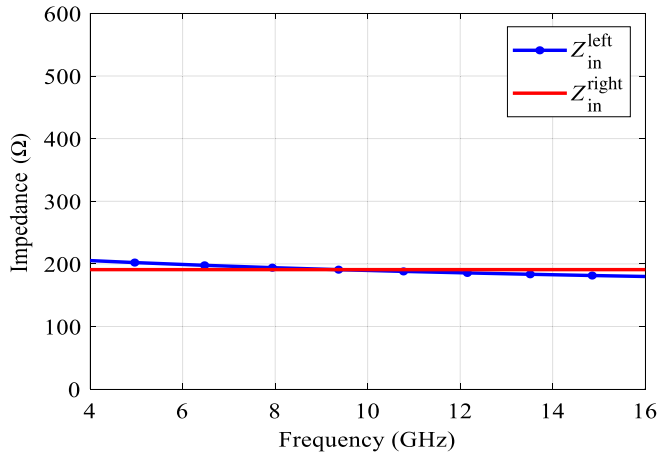


FIG. 19. Curves of  $Z_{in}^{right}$  and  $Z_{in}^{left}$ .

satisfactions of Eq. (7). The unit cells for the support of TE mode and their complementary unit cells for the support of TM mode are displayed in Fig. 15. The unit cells whose dimensions are smaller than the operational wavelength ( $\lambda$ ) are arranged in the lattice periodic structure. The geometrical parameters of the unit cells of regions I, II, and III with scheme configurations shown in Fig. 15 are as follows:  $P_x = 1.3$  mm,  $P_y = 2.7$  mm,  $a_1 = 0.45$  mm,  $b_1 = 1.05$  mm,  $a_2 = 0.2$  mm,  $b_2 = 0.48$  mm,  $a_3 = 0.2$  mm,  $b_3 = 0.39$  mm, and  $S = 0.2$  mm. The substrate is a 20-mil-thick Rogers RT \duriod 6010 whose dielectric constant is 10.5 and is used for the ungrounded unit cells. The equivalent circuit model of the Y splitter is observed in Fig. 15(b). The input and output transitions and coaxial lines as feed sources and regions I, II, and III are modeled as transmission lines with the characteristic impedances  $Z_{0,I}$ ,  $Z_{0,II}$ , and  $Z_{0,III}$ .

Although the existence of bends and discontinuities in the wave path cause the diffraction and leakage, it seems that this leakage can be decreased by changing

the propagation impedance of TM and TE surfaces along the interface for the LW mode. Considering the bends and discontinuities of the proposed Y-splitter impedance-matching techniques must be applied to prevent the diffraction and leakage. For impedance matching at the junction of regions I and II as labeled in Fig. 15(b), the following relations should hold  $Z_{in}^{left} = Z_{in}^{right}$  [24]

$$Z_{0,III} = Z_{0,II}, \quad (17)$$

$$Z_{0,I} = \frac{1}{2}Z_{0,II}. \quad (18)$$

These relations hold in the case that there is impedance matching at the input and output ports. In order to investigate the impedance matching between regions I and II, the characteristic impedance of each region should be obtained (namely  $Z_{0,I}$ ,  $Z_{0,II}$ , and  $Z_{0,III}$ ). The curves of the characteristic impedances of three regions as functions of the dimensions of their patches can be determined similar to the method of the calculation of the characteristic impedance of waveguide III. The unit cells of regions I, II, and III are presented in Fig. 16. The parameters  $P_I = 2.7$  mm,  $P_{II} = 1.85$  mm,  $P_{III} = 2.7$  mm denote the periods. Figure 11(a) shows the characteristic impedance of region I ( $Z_{0,I}$ ) as a function of the dimensions of its patches ( $a_1, b_1$ ).  $Z_{0,II}$  as a function of  $a_2, b_2$ , and  $Z_{0,III}$  as a function of  $a_3, b_3$ , which are extracted by the eigenmode solver of ANSYS HFSS software can be seen in Figs. 17(b) and 17(c).

Figure 17 demonstrates that the value of characteristic impedance of each region has an inverse relationship with the dimensions of its patches. Noting that for impedance matching between regions I, II, and III, the characteristic impedances of regions II and III should be larger than that of region I, the Y splitter is designed as follows. First, (considering the fabrication limitation of the lowest spacing between patches of 0.2 mm) the parameters  $a_1 = 0.45$  mm,  $b_1 = 1.05$  mm are selected for region I. Now, by knowing the value of  $a_1$  and  $b_1$  for this region, its characteristic

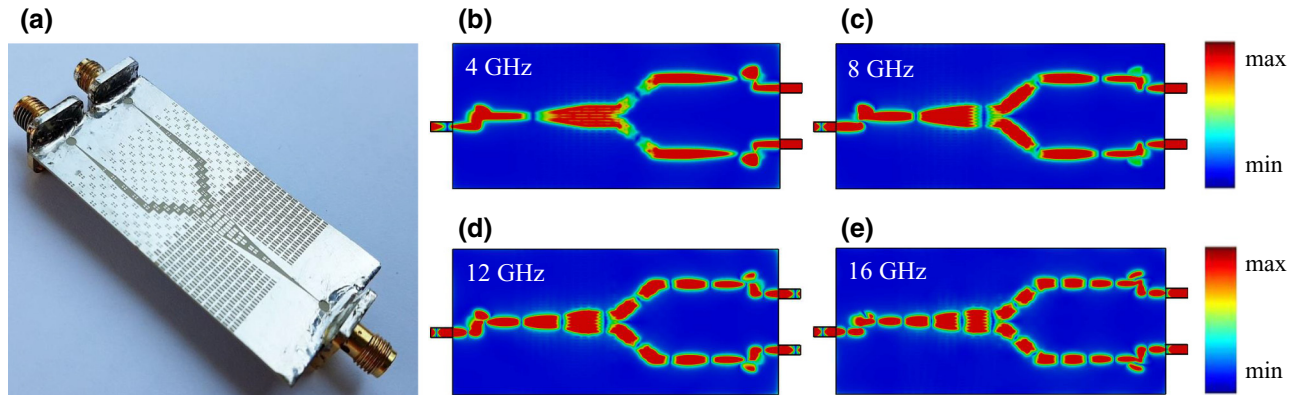


FIG. 20. (a) Fabricated prototype impedance-interface Y splitter. (b) Simulated electric field distribution at 4 GHz. (c) Simulated electric field distribution at 8 GHz. (d) Simulated electric field distribution at 12 GHz. (e) Simulated electric field distribution at 16 GHz.

impedance can be calculated by simulation and Eq. (5). Then the values of the characteristic impedances of regions II and III are computed by Eqs. (17) and (18). By selecting the values of  $a_2 = a_3 = 0.2$  mm for regions II and III, the values of  $b_2$  and  $b_3$  should be obtained so that their characteristic impedances are equal. The optimum dimensions are determined by CST Microwave Studio as  $b_2 = 0.48$  mm,  $b_3 = 0.39$  mm. Obviously, various values of dimensions of patches may satisfy Eqs. (17) and (18). However, the optimum values are those obtained above.

The curves of the characteristic impedances of three regions are illustrated in Fig. 18. The curves of  $Z_{in}^{right}$  and  $Z_{in}^{left}$  are presented versus frequency in Fig. 19. The perfect matching occurs wherever they are equal. The separation of these curves lead to a mismatch, which causes some reflection of waves at the boundary between regions I, II and some leakage enhancement. These diagrams are evaluated by the assumptions of homogeneous and lossless metasurface, perfect matching of input and output terminals, and electromagnetic TE-like mode. Consequently,

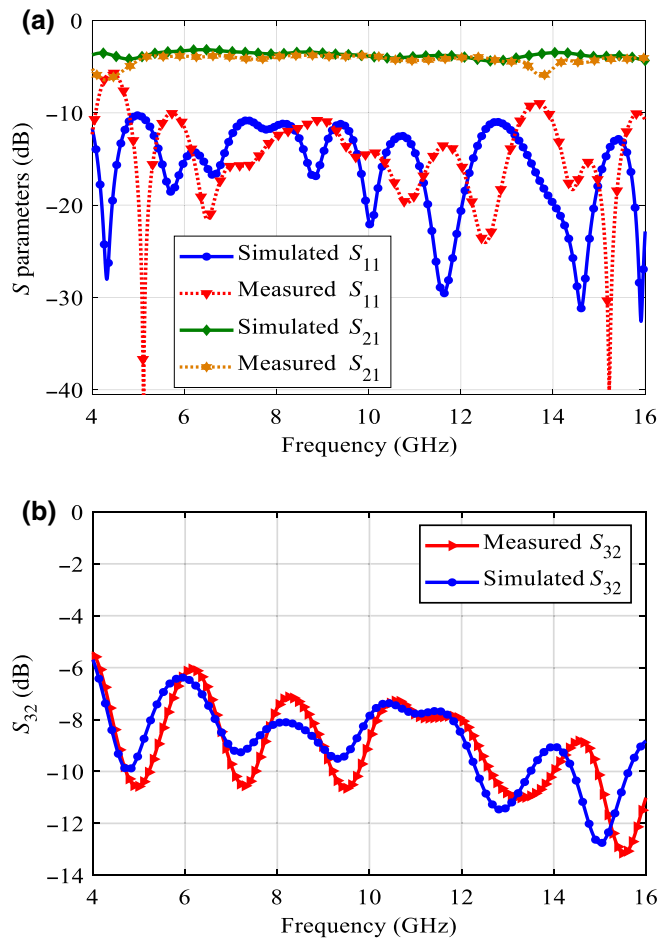


FIG. 21. (a) Simulated and measured diagrams of scattering parameters  $S_{11}$  and  $S_{21}$ . (b) Simulation and experimental isolation ( $S_{32}$ ) between the output ports.

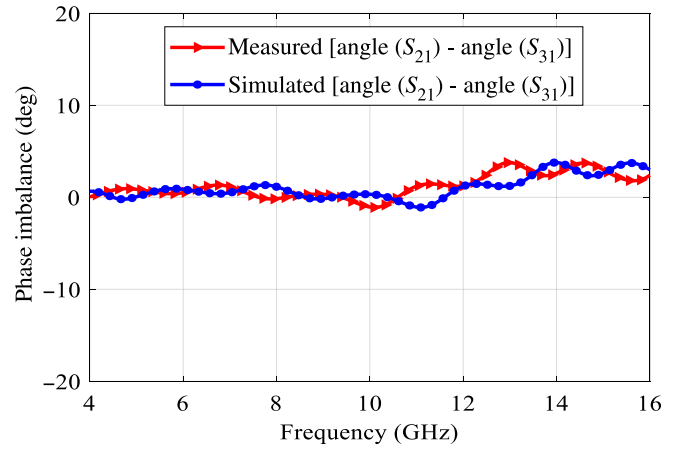


FIG. 22. Simulation and experimental phase imbalances of the output ports.

some discrepancy is evidently expected between the values of  $Z_{in}^{right}$  and  $Z_{in}^{left}$ .

#### IV. FABRICATION RESULTS

For the proof of concept, the designed Y splitter is fabricated and measured as shown in Fig. 20(a). The electric field distribution at 4, 8, 12, and 16 GHz are illustrated in Figs. 20(b)–20(e). Also, the simulated and measured diagrams of scattering parameters  $S_{11}$  and  $S_{21}$  are presented in Fig. 21(a). As shown in Fig. 21(a), the measurement data are consistent with the simulation results. However, observe that these two frequency responses do not exactly coincide. The differences between the simulation results and the measurement data are due to the fabrication tolerances and the limitation of connectors and would reduce by better workmanship. The isolation ( $S_{32}$ ) between the output ports is illustrated in Fig. 21(b). The phase imbalance diagram for the proposed Y splitter in the frequency band 4–16 GHz can be seen in Fig. 22. Due to its geometrical symmetry, the output phase is equal for both output ports. However, the experimental results show the broadband performance of the Y splitter in the frequency range of 4–16 GHz with the FBW of 120% as well as low-loss and in-phase outputs.

#### V. CONCLUSION

In this work, a compact, low-loss, and broadband TE-TM impedance-interface waveguide and a Y splitter (based on the complementary impedance surfaces) are presented. Also a broadband mode-matching technique to design transition for the conversion of TEM modes to LW modes is proposed. We show that the introduced wideband Vivaldi transition can be used for the connection of conventional microwave waveguides and impedance-interface waveguides. The key advantages of the proposed devices are



high confinement, low-loss power transmission, broad bandwidth, and easy fabrication. Our work has led us to conclude that LW modes have the capability of being implemented in microwave to optical frequency bands.

- 
- [1] John Polo, Tom Mackay, and Akhlesh Lakhtakia, *Electromagnetic Surface Waves: A Modern Perspective* (Elsevier, Amsterdam, 2013).
- [2] Simon Laurette, Anthony Treizebre, and Bertrand Bocquet, Corrugated Goubau lines to slow down and confine THz waves, *IEEE Trans. Terahertz Sci. Technol.* **2**, 340 (2012).
- [3] Zhixia Xu, Shunli Li, Xiaoxing Yin, Hongxin Zhao, and Leilei Liu, Radiation loss of planar surface plasmon polaritons transmission lines at microwave frequencies, *Sci. Rep.* **7**, 6098 (2017).
- [4] Yury G. Smirnov and Dmitry V. Valovik, Guided electromagnetic waves propagating in a plane dielectric waveguide with nonlinear permittivity, *Phys. Rev. A* **91**, 013840 (2015).
- [5] Uwe Langbein, Falk Lederer, and Hans-Ernst Ponath, Generalized dispersion relations for nonlinear slab-guided waves, *Opt. Commun.* **53**, 417 (1985).
- [6] Christopher L. Holloway, Edward F. Kuester, Joshua A. Gordon, John O'Hara, Jim Booth, and David R. Smith, An overview of the theory and applications of metasurfaces: The two-dimensional equivalents of metamaterials, *IEEE Antennas Propag. Mag.* **54**, 10 (2012).
- [7] F. Ramos-Mendieta and P. Halevi, Electromagnetic surface modes of a dielectric superlattice: The supercell method, *JOSA B* **14**, 370 (1997).
- [8] Hongyu Shi, Jianxing Li, Anxue Zhang, Yansheng Jiang, Jiafu Wang, Zhuo Xu, and Song Xia, Gradient metasurface with both polarization-controlled directional surface wave coupling and anomalous reflection, *IEEE Antennas Wirel. Propag. Lett.* **14**, 104 (2014).
- [9] Xiang Wan, Yun Bo Li, Ben Geng Cai, and Tie Jun Cui, Simultaneous controls of surface waves and propagating waves by metasurfaces, *Appl. Phys. Lett.* **105**, 121603 (2014).
- [10] Ryan Quarfoth and Daniel Sievenpiper, Artificial tensor impedance surface waveguides, *IEEE Trans. Antennas Propag.* **61**, 3597 (2013).
- [11] Amit M. Patel and Anthony Grbic, A printed leaky-wave antenna based on a sinusoidally-modulated reactance surface, *IEEE Trans. Antennas Propag.* **59**, 2087 (2011).
- [12] Francis Elek, Brian B. Tierney, and Anthony Grbic, Synthesis of tensor impedance surfaces to control phase and power flow of guided waves, *IEEE Trans. Antennas Propag.* **63**, 3956 (2015).
- [13] Christopher R. Williams, Steven R. Andrews, S. A. Maier, A. I. Fernández-Domínguez, L. Martín-Moreno, and F. J. García-Vidal, Highly confined guiding of terahertz surface plasmon polaritons on structured metal surfaces, *Nat. Photonics* **2**, 175 (2008).
- [14] Mei Li, Shaoqiu Xiao, Jiang Long, and Daniel F. Sievenpiper, Surface waveguides supporting both tm mode and te mode with the same phase velocity, *IEEE Trans. Antennas Propag.* **64**, 3811 (2016).
- [15] Xianghong Kong, Dia'aaldin J. Bisharat, Gaobiao Xiao, and Daniel F. Sievenpiper, Analytic theory of an edge mode between impedance surfaces, *Phys. Rev. A* **99**, 033842 (2019).
- [16] Dia'aaldin J. Bisharat and Daniel F. Sievenpiper, Guiding Waves along an Infinitesimal Line between Impedance Surfaces, *Phys. Rev. Lett.* **119**, 106802 (2017).
- [17] Zhixia Xu, Xiaoxing Yin, and Daniel F. Sievenpiper, Adiabatic Mode-Matching Techniques for Coupling between Conventional Microwave Transmission Lines and One-Dimensional Impedance-Interface Waveguides, *Phys. Rev. Appl.* **11**, 044071 (2019).
- [18] Simon Ramo, John R. Whinnery, and Theodore Van Duzer, *Fields and Waves in Communication Electronics* (John Wiley & Sons, India, 2008).
- [19] Roger F. Harrington, *Time-Harmonic Electromagnetic Fields* (McGraw-Hill, New York, 1961).
- [20] Xiao Li, Fan Yang, Maokun Li, and Shenheng Xu, Generalized boundary conditions in surface electromagnetics: Fundamental theorems and surface characterizations, *Appl. Sci.* **9**, 1891 (2019).
- [21] Dia'aaldin J. Bisharat and Daniel F. Sievenpiper, Manipulating line waves in flat graphene for agile terahertz applications, *Nanophotonics* **7**, 893 (2018).
- [22] Olli Luukkonen, Constantin Simovski, Gérard Granet, George Goussetis, Dmitri Lioubtchenko, Antti V. Raisanen, and Sergei A. Tretyakov, Simple and accurate analytical model of planar grids and high-impedance surfaces comprising metal strips or patches, *IEEE Trans. Antennas Propag.* **56**, 1624 (2008).
- [23] David González-Ovejero, Enrica Martini, and Stefano Maci, Surface waves supported by metasurfaces with self-complementary geometries, *IEEE Trans. Antennas Propag.* **63**, 250 (2014).
- [24] David M. Pozar, *Microwave Engineering 3e* (Wiley, New York, 2006).
- [25] Amit M. Patel and Anthony Grbic, Effective surface impedance of a printed-circuit tensor impedance surface (PCTIS), *IEEE Trans. Microw. Theory Tech.* **61**, 1403 (2013).
- [26] Amin Kianinejad, Zhi Ning Chen, and Cheng-Wei Qiu, Low-loss spoof surface plasmon slow-wave transmission lines with compact transition and high isolation, *IEEE Trans. Microw. Theory Tech.* **64**, 3078 (2016).
- [27] Steven G. Johnson, Peter Bienstman, M. A. Skorobogatiy, Mihai Ibanescu, Eleftherios Lidorikis, and J. D. Joannopoulos, Adiabatic theorem and continuous coupled-mode theory for efficient taper transitions in photonic crystals, *Phys. Rev. E* **66**, 066608 (2002).
- [28] Hui Feng Ma, Xiaopeng Shen, Qiang Cheng, Wei Xiang Jiang, and Tie Jun Cui, Broadband and high-efficiency conversion from guided waves to spoof surface plasmon polaritons, *Laser Photon. Rev.* **8**, 146 (2014).
- [29] Hao Chi Zhang, Shuo Liu, Xiaopeng Shen, Lin Hui Chen, Lianming Li, and Tie Jun Cui, Broadband amplification of spoof surface plasmon polaritons at microwave frequencies, *Laser Photon. Rev.* **9**, 83 (2015).
- [30] Di Cao, Yujian Li, and Junhong Wang, Wideband compact slotline-to-spoof-surface plasmon-polaritons transition for millimeter waves, *IEEE Antennas Wirel. Propag. Lett.* **16**, 3143 (2017).